International Journal of Non-Linear Mechanics 127 (2020) 103595

Contents lists available at ScienceDirect

International Journal of Non-Linear Mechanics

journal homepage: www.elsevier.com/locate/nlm

Measurement of the Poisson's ratio and Young's modulus of an isotropic material with T-shape contact resonance atomic force microscopy

Feifei Gao, Yin Zhang *

State Key Laboratory of Nonlinear Mechanics, Institute of Mechanics, Chinese Academy of Sciences, Beijing 100190, China
School of Engineering Science, University of Chinese Academy of Sciences, Beijing 100049, China

ARTICLE INFO

Keywords:
Mode coupling
Bifurcation
Curve veering
Poisson's ratio
Young's modulus

ABSTRACT

The Poisson's ratio and the Young's modulus play an important role in the characterization of nanomaterial mechanical properties. They are the vital parameters of understanding nanoscale material behavior. Here we report a method of quantitatively determining the values of the Poisson's ratio and the Young's modulus with a T-shape contact resonance atomic force microscopy. Unlike the cantilever of a traditional atomic force microscopy, the flexural and torsional modes of the T-shape cantilever are simultaneously excited and coupled in the contact mode. Through the analysis, the bifurcation of the coupled contact resonance frequencies is found in higher modes with the increasing contact stiffness. More importantly, the frequency bifurcation point can be used to decouple the Poisson's ratio and the Young's modulus, which leads to the determination of their separate values. In contrast to the previous methods, in which the Poisson's ratio and the Young's modulus are intrinsically coupled and there is no effective way of decoupling, the method presented in this study offers a new way of decoupling and determining these two parameters. This efficient and accurate method can be of significant help to the characterization of various nanomaterials.

1. Introduction

With the rapid development of nanomaterials, the characterization of the nanoscale material properties, such as the friction [1], modulus [2], adhesion [3], is indispensable. The sample properties can change dramatically with the decrease of size and the increase of surface to volume ratio [4,5]. Therefore, a method which can quantitatively characterize the small-scale material properties is crucial. The Poisson's ratio and the Young's modulus are important parameters of characterizing the nanomaterial mechanical properties. They provide insights into the behavior of nanoscale material. For example, Poisson's ratio is a crucial parameter in the wrinkling behavior of a uniaxially stretched thin sheet [6].

The bulge/blister tests [7] and nanoindentation (NI) technology [8–11] are extensively used because of their easiness and effectiveness. The bulge/blister tests are frequently used to extract thin film mechanical properties. On the other hand, the mechanical properties, such as hardness, modulus, fracture toughness, can be obtained from the indentation force-distance curve [8]. However, the static NI technology is not applicable for many soft materials due to its destructiveness. A solution is to use the dynamic NI, which can nondestructively measure the continuous stiffness of a soft sample [12]. However, these technologies have a major deficiency that Poisson's ratio and Young's modulus cannot be individually obtained [13].

The technology based on atomic force microscopy (AFM) [14] is another common method to character the properties of nanoscale material. The high spatial resolution and imaging capabilities of AFM are more suitable for the nanoscale materials characterization [4]. The contact resonance technology is one of the AFM methods that provide mechanical property information. Compared with the tapping mode, the contact resonance technology is more suitable for characterizing various materials, typically with the modulus ranging from 1 GPa to 300 GPa [4]. Various models have been developed to understand the cantilever motion in contact resonance force microscope (CRFM) [15–18]. Many significant results are also achieved by CRFM, for example, the quantitative characterization of the mechanical properties of the various materials [19–22], and the subsurface structure [23–27]. Using CRFM, Hurley et al. detected the subsurface particles and the substrate/film adhesion [3]. The local internal friction and the beginning of plasticity were also observed by CRFM [1]. However, there still remains a major challenge in obtaining the separate values of the Poisson's ratio and the Young's modulus.

In the previous studies on contact resonance technology, both the theoretical and experimental researches, mainly focus on the flexural/bending mode of a CRFM cantilever [1–4,15,19,21–23]. The role of the torsional mode in obtaining the separate Poisson's ratio and Young's modulus is not fully explored or even overlooked. In a wide frequency

* Corresponding author at: State Key Laboratory of Nonlinear Mechanics, Institute of Mechanics, Chinese Academy of Sciences, Beijing 100190, China.
E-mail address: zhangyin@lnm.imech.ac.cn (Y. Zhang).

https://doi.org/10.1016/j.ijnonlinmec.2020.103595
Received 17 March 2020; Received in revised form 2 August 2020; Accepted 25 August 2020
Available online 27 August 2020
0020-7462/

range, the torsional vibration is larger than the flexural one [28], i.e., the torsional vibration is more sensitive. Hurley et al. obtained the Poisson's ratio by an experiment that simultaneously measures the flexural and torsional contact resonance frequencies under the same experimental conditions [2], but the experiment is rather complicated. A torsional harmonic cantilever (THC) was proposed by Sahin et al. [28]. In THC, the flexural and torsional modes can be excited at the same time because the tip is off the center axis of the cantilever. A torque is generated due to the tip–sample interactions together with the above off-center geometric configuration. The THC in Sahin's study works in tapping mode, the flexural and torsional vibrations can be separately extracted. However, in the contact mode the flexural and the torsional vibrations are coupled, which still poses a significant challenge for analysis.

In this study, we present an inverse problem-solving method to obtain the separate values of the Poisson's ratio and the Young's modulus by designing a T-shape contact resonance atomic force microscopy. Similar to the THC [28], the tip is off the center axis of the T-shape cantilever. The flexural and torsional modes are simultaneously excited when the tip is in contact with a sample. And a coupled mode of the flexural and torsional vibrations is obtained, which leads to a resonance frequency bifurcation in higher modes with the increasing contact stiffness. The inverse problem-solving method presented here in essence is to determine the Poisson's ratio and Young's modulus separately by the bifurcation point. This efficient and accurate method provides an insight into the characterization of various nanomaterials.

2. Model development

As shown in Fig. 1, the T-shape cantilever consists of two parts, which have different lengths and widths of b_i and L_i ($i = 1$ and 2). Subscript 1 denotes the parameters of the narrow part connected with the fixed end, and subscript 2 denotes the parameters of the wider part connected with the free end. The two parts are with the same thickness h. The total length is $L = L_1 + L_2$. The tip is at the free end and off the cantilever center axis with the distance of d. The height of the tip is H. Here, $\theta(x,t)$ denotes the twist angle of the cantilever.

For the T-shape cantilever, because the tip is off the center axis, the flexural and torsional modes are excited at the same time when tip is in contact with sample. Here the Euler–Bernoulli beam theory is used [4]. The vibration of a T-shape cantilever is described by the following equations, which is derived by applying the Hamilton's principle [29].

$$\begin{cases} m_1 \dfrac{\partial^2 w_1}{\partial t^2} + EI_1 \dfrac{\partial^4 w_1}{\partial x^4} = 0, & 0 \le x \le L_1, \\ m_2 \dfrac{\partial^2 w_2}{\partial t^2} + EI_2 \dfrac{\partial^4 w_2}{\partial x^4} = 0, & L_1 \le x \le L. \end{cases} \tag{1}$$

$$\begin{cases} \rho I_{P1} \dfrac{\partial^2 \theta_1}{\partial t^2} = GJ_1 \dfrac{\partial^2 \theta_1}{\partial x^2}, & 0 \le x \le L_1, \\ \rho I_{P2} \dfrac{\partial^2 \theta_2}{\partial t^2} = GJ_2 \dfrac{\partial^2 \theta_2}{\partial x^2}, & L_1 \le x \le L. \end{cases} \tag{2}$$

where w_i, θ_i, m_i, EI_i, ρ, I_{Pi}, GJ_i ($i = 1$ and 2) are the cantilever deflection, angle of twist, mass per unit length, flexural stiffness, density, polar area moment of the inertia and torsional stiffness of the two parts, respectively. The polar area moment of the inertia $I_{Pi} = (b_i h^3 + b_i^3 h)/12$ ($i = 1$ and 2), and the torsional stiffness $GJ_i = \frac{1}{3} G b_i h^3 \left[1 - 0.63\frac{h}{b_i} + 0.052\left(\frac{h}{b_i}\right)^3\right]$ ($i = 1$ and 2) [30].

Here, the discussion is limited to isotropic materials. By applying Hamilton's principle, the boundary conditions at ($x = 0$ and L) in Fig. 1 are derived as follows:

$$w_1(0,t) = w_1'(0,t) = 0, \quad EI_2 w_2''(L,t) = 0, \quad \theta_1(0,t) = 0. \tag{3}$$

The coupled boundary conditions at $x = L$ are now derived as follows:

$$\begin{aligned} &EI_2 w_2'''(L,t) = k_n \left[w_2(L,t) - \theta_2(L,t)d\right], \\ &GJ_2 \theta_2'(L,t) = -k_n d\, w_2(L,t) - k_L H^2 \theta_2(L,t). \end{aligned} \tag{4}$$

where the vertical contact stiffness k_n and the tangential contact stiffness k_L are given by $k_n = 2E^* a$ [31] and $k_L = 8G^* a$ [32], respectively. For isotropic materials, the reduced system modulus E^* is defined as $\frac{1}{E^*} = \frac{1-\upsilon_t^2}{E_t} + \frac{1-\upsilon_s^2}{E_s}$ [2,31] and G^* is defined as $\frac{1}{G^*} = \frac{2-\upsilon_t}{G_t} + \frac{2-\upsilon_s}{G_s}$ [2,32], the subscripts "t" and "s" denote tip and sample, respectively. In the Hertzian contact, the contact radius a is given by $a = (3RF_N/4E^*)^{1/3}$ [2, 31]. Here R is the tip radius curvatures and F_N is the applied force normal to the surface.

Besides the boundary conditions of Eqs. (3) and (4), the following equations at $x = L_1$ are also derived:

$$\begin{aligned} &w_1(L_1,t) = w_2(L_1,t) \quad w_1'(L_1,t) = w_2'(L_1,t) \quad EI_1 w_1''(L_1,t) = EI_2 w_2''(L_1,t), \\ &EI_1 w_1'''(L_1,t) = EI_2 w_2'''(L_1,t), \quad \theta_1(L_1,t) = \theta_2(L_1,t), \\ &GJ_1 \theta_1'(L_1,t) = GJ_2 \theta_2'(L_1,t). \end{aligned} \tag{5}$$

Physically, these equations are to ensure the continuity of the displacement, slope, bending moment, shear, angle and torsional moment at $x = L_1$.

The following quantities are introduced to nondimensionalize Eqs. (1) and (2)

$$\xi = x/L, \quad \xi_o = L_1/L, \quad W_1 = w_1/L, \quad W_2 = w_2/L, \quad \tau = \sqrt{EI_1/m_1 L^4}\, t. \tag{6}$$

where $\sqrt{EI_1/m_1 L^4}$ is with the unit of Hertz and it is the same order of the first natural frequency of a uniform and undamped cantilever [33]. Eqs. (1) and (2) now become the following dimensionless ones:

$$\begin{cases} \dfrac{\partial^2 W_1}{\partial \tau^2} + \dfrac{\partial^4 W_1}{\partial \xi^4} = 0, & \dfrac{\partial^2 \theta_1}{\partial \xi^2} = \beta_1 \dfrac{\partial^2 \theta_1}{\partial \tau^2}, & 0 \le \xi \le \xi_o, \\ \dfrac{\partial^2 W_2}{\partial \tau^2} + \dfrac{\partial^4 W_2}{\partial \xi^4} = 0, & \dfrac{\partial^2 \theta_2}{\partial \xi^2} = \beta_1 \beta_2 \dfrac{\partial^2 \theta_2}{\partial \tau^2}, & \xi_o \le \xi \le 1. \end{cases} \tag{7}$$

Here $\beta_1 = \frac{EI_1/L^3}{\rho A_1 L} \frac{\rho I_{P1} L}{GJ_1/L}$. The flexural and torsional wave numbers, γ and η, are related with the following dispersion relations $\omega^2 = \gamma^4 \frac{EI_1/L^3}{\rho A_1 L} = \eta^2 \frac{GJ_1/L}{\rho I_{P1} L}$ [5]. ω is the angular frequency. Therefore, $\eta = \sqrt{\beta_1}\gamma^2$, and parameter $\sqrt{\beta_1}$ determines the likelihood of the mode coupling. Here β_2 is the ratio of the polar area moment of the inertia to the torsional stiffness defined as $\beta_2 = \frac{I_{P2}}{I_{P1}} \frac{GJ_1}{GJ_2}$.

The solution forms of Eq. (7) are assumed as follows:

$$W_i(\xi,\tau) = Y_i(\xi) e^{i\omega\tau}, \quad \theta_i(\xi,\tau) = \psi_i(\xi) e^{i\omega\tau}, \quad (i = 1 \text{ and } 2). \tag{8}$$

The following mode shapes of the T-shape cantilever are obtained by substituting Eq. (8) into Eq. (7).

$$\begin{cases} Y_1(\xi) = A_1 \cos(\lambda_f \xi) + B_1 \sin(\lambda_f \xi) + C_1 \cosh(\lambda_f \xi) + D_1 \sinh(\lambda_f \xi), & 0 \le \xi \le \xi_o, \\ Y_2(\xi) = A_2 \cos(\lambda_f \xi) + B_2 \sin(\lambda_f \xi) + C_2 \cosh(\lambda_f \xi) + D_2 \sinh(\lambda_f \xi), & \xi_o \le \xi \le 1, \\ \psi_1(\xi) = A_3 \cos(\lambda_t \xi) + B_3 \sin(\lambda_t \xi), & 0 \le \xi \le \xi_o, \\ \psi_2(\xi) = A_4 \cos(\sqrt{\beta_2}\lambda_t \xi) + B_4 \sin(\sqrt{\beta_2}\lambda_t \xi), & \xi_o \le \xi \le 1. \end{cases} \tag{9}$$

Here $\lambda_f = \sqrt{\omega}$, $\lambda_t = \sqrt{\beta_1}\omega$, and they are related with $\lambda_t = \sqrt{\beta_1}\lambda_f^2$. And, A_i, B_i, C_i, D_i are the constants to be determined. The corresponding dimensionless equations of Eqs. (3)–(5) are

$$\begin{aligned} &Y_1(0) = Y_1'(0) = Y_2''(1) = 0, \quad \psi_1(0) = 0, \quad Y_2(1) = \alpha_1 \left[Y_2(1) - \alpha_2 \psi_2(1)\right], \\ &\psi_2(1) = -\alpha_1 \alpha_2 \beta_3 Y_2(1) - \alpha_3^2 \alpha_4 \psi_2(1), \quad Y_1(\xi_o) = Y_2(\xi_o), \quad Y_1'(\xi_o) = Y_2'(\xi_o), \\ &Y_1''(\xi_o) = \zeta Y_2''(\xi_o), \quad Y_1'''(\xi_o) = \zeta Y_2'''(\xi_o), \quad \psi_1(\xi_o) = \psi_2(\xi_o), \\ &\psi_1'(\xi_o) = \kappa \psi_2'(\xi_o). \end{aligned} \tag{10}$$

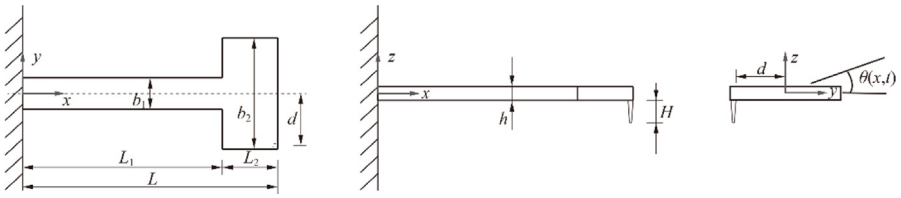

Fig. 1. Schematic diagram of the AFM T-shape cantilever dimensions.

Here ζ is a width ratio of the two parts defined as $\zeta = b_2/b_1$. $\beta_3 = EI_2/GJ_2$ indicates the ratio of the flexural stiffness to the torsional stiffness. $\kappa = GJ_2/GJ_1$ is the torsional stiffness ratio of the two parts. And dimensionless α_i's ($i = 1$ to 4) are defined as

$$\alpha_1 = k_n L^3/EI_2, \quad \alpha_2 = d/L, \quad \alpha_3 = H/L, \quad \alpha_4 = k_L L^3/GJ_2. \tag{11}$$

Physically α_1 is the ratio of the vertical contact stiffness to the cantilever flexural stiffness and α_4 is the ratio of the tangential contact stiffness to the cantilever torsional stiffness. Here α_2 is the ratio of the off-center distance to the total cantilever length. And α_3 is the ratio of the tip height to the total cantilever length.

Substituting Eq. (10) into Eq. (9), we obtain twelve equations. These twelve equations can be rewritten as $\mathbf{AV} = 0$. Here $\mathbf{A}$ is a 12×12 matrix, and $\mathbf{V} = \begin{bmatrix} A_1 & B_1 & C_1 & D_1 & A_2 & B_2 & C_2 & D_2 & A_3 & B_3 & A_4 & B_4 \end{bmatrix}^T$. The resonance frequencies of the T-shape cantilever are obtained by setting the determinant of matrix $\mathbf{A}$ to be zero, i.e., $|\mathbf{A}| = 0$ [34]. The above matrix $\mathbf{A}$ can be rewritten as $\mathbf{A} = \begin{pmatrix} \mathbf{B} & \mathbf{C} \\ \mathbf{D} & \mathbf{E} \end{pmatrix}$. $\mathbf{B}$, $\mathbf{C}$, $\mathbf{D}$ and $\mathbf{E}$ are sub-matrices defined in Appendix A. As shown in Appendix A, the $|\mathbf{A}| = 0$ is equivalent to the $\left|\mathbf{E} - \mathbf{DB}^{-1}\mathbf{C}\right| = 0$, which leads to the following equation

$$f_1(\alpha_1, \lambda_f) - f_2(\lambda_f) = 0 \tag{12}$$

Here the $f_1(\alpha_1, \lambda_f)$ is a function of both the contact stiffness and the contact resonance frequency, and the $f_2(\lambda_f)$ is a function of contact resonance frequency. The expressions of $f_1(\alpha_1, \lambda_f)$ and $f_2(\lambda_f)$ are given in Appendix A.

3. Results and discussion

In the contact mode, the flexural and torsional modes are coupled. The contact resonance frequencies are influenced by many variable parameters, such as the contact stiffness, tip position, geometrical parameters of cantilever, properties of sample. And α_1 and α_4 are two parameters related with the Poisson's ratio and the Young's modulus. Therefore, we aim to obtain the separate values of the Poisson's ratio and the Young's modulus by examining the relation between the resonance frequency and these two parameters. Here $\alpha_1 = k_n L^3/EI_2$, $\alpha_4 = k_L L^3/GJ_2$. The following figures were calculated by assuming the total length $L = 300$ μm, the width $b_2 = 50$ μm, the thickness $h = 3$ μm, the offset distance $d = 24$ μm and the length ratio $\xi_o = 0.9$. The width ratio ζ of the cantilever is 2.5 except Fig. 6. The tip is silicon with $E_t = 160.5$ GPa and $\upsilon_t = 0.168$ [2].

A geometric analysis method is used to qualitatively analyze the relation between the contact resonance frequency ($\omega = \lambda_f^2$) and the α_1 from Eq. (12). Fig. 2 shows the contact resonance frequency ($\omega = \lambda_f^2$) is as a function of α_1. Here $\alpha_1 = k_n L^3/EI_2$, $k_n = 2E^* a$, as defined in Eq. (4), $*$ is the vertical contact stiffness, which is proportional to the square root of the indentation depth. In Fig. 2, each intersection of $f_1(\alpha_1, \lambda_f)$ and $f_2(\lambda_f)$ corresponds to a resonance frequency as indicated by Eq. (12). The first two resonance frequencies increase continuously with the increasing α_1. However, the resonance frequency loses stability from the third mode, which suddenly reaches a higher value at a certain α_1. As seen in Fig. 2, when α_1 is less than 60, the third intersection of $f_1(\alpha_1, \lambda_f)$ and $f_2(\lambda_f)$ corresponds to the resonance frequency ($\lambda_f = \sqrt{\omega}$)

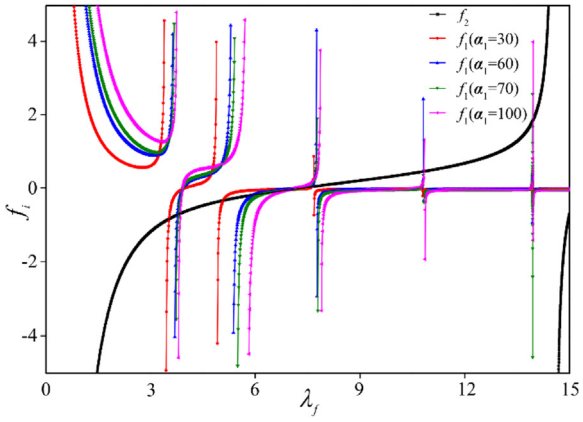

Fig. 2. Variation of the function f_i with frequency for different α_1. Where the function $f_1(\alpha_1, \lambda_f)$ and $f_2(\lambda_f)$ are given by Eq. (12), and the intersection points of $f_1(\alpha_1, \lambda_f)$ and $f_2(\lambda_f)$ indicate the contact resonance frequencies ($\omega = \lambda_f^2$) of the T - shape cantilever. The figure is obtained by a geometric analysis, and shows the contact resonance frequency of the T – shape cantilever.

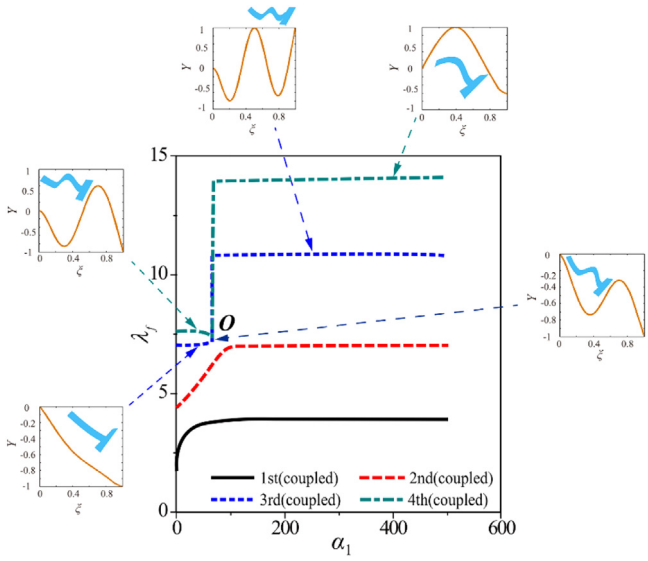

Fig. 3. Contact resonance frequencies ($\omega = \lambda_f^2$) as a function of α_1. The insets are the corresponding mode shapes at different α_1s.

ranging from 6 to 9. In comparison, the resonance frequency is higher than 10 when α_1 is larger than 70. This sudden change of behavior is more straightforwardly shown in Fig. 3 as the relation of the resonance frequency ω (λ_f^2) versus α_1.

The numerical solutions to the resonance frequencies of the T-shape cantilever as a function of α_1 are presented in Fig. 3. The curves are the resonance frequencies of the first to the fourth modes from the bottom up. As seen in Fig. 3, the third resonance frequency of the T-shape cantilever increases continuously with the increasing α_1 until

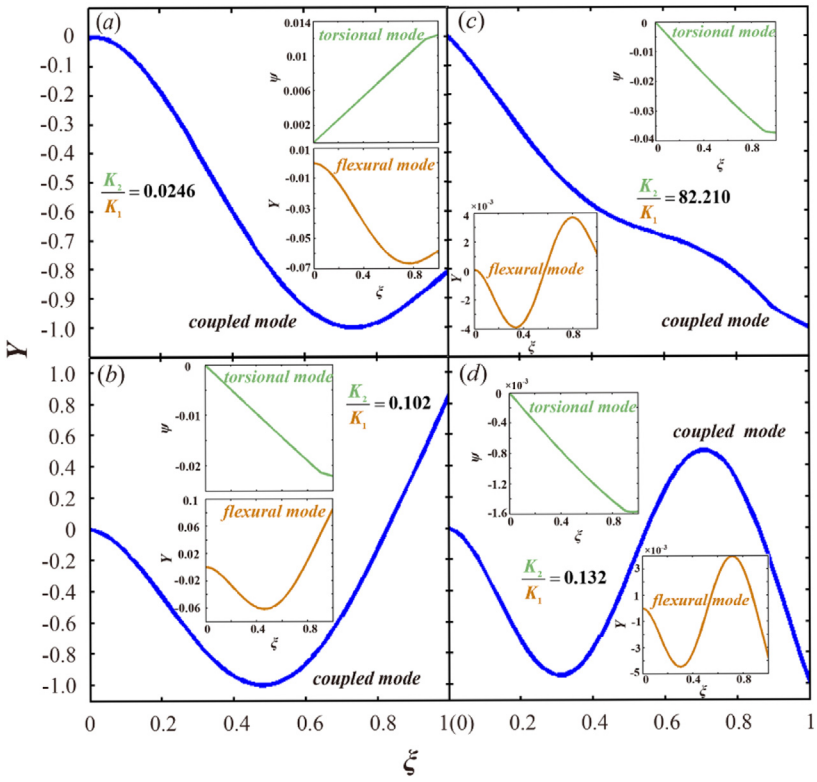

Fig. 4. The first four mode shapes with $\alpha_1 = 20$ ((a) the first mode, (b) the second mode, (c) the third mode, (d) the fourth mode). The large diagrams are the contact resonance mode shapes, the orange insets are the flexural mode shapes, and the green insets are the torsional mode shapes.

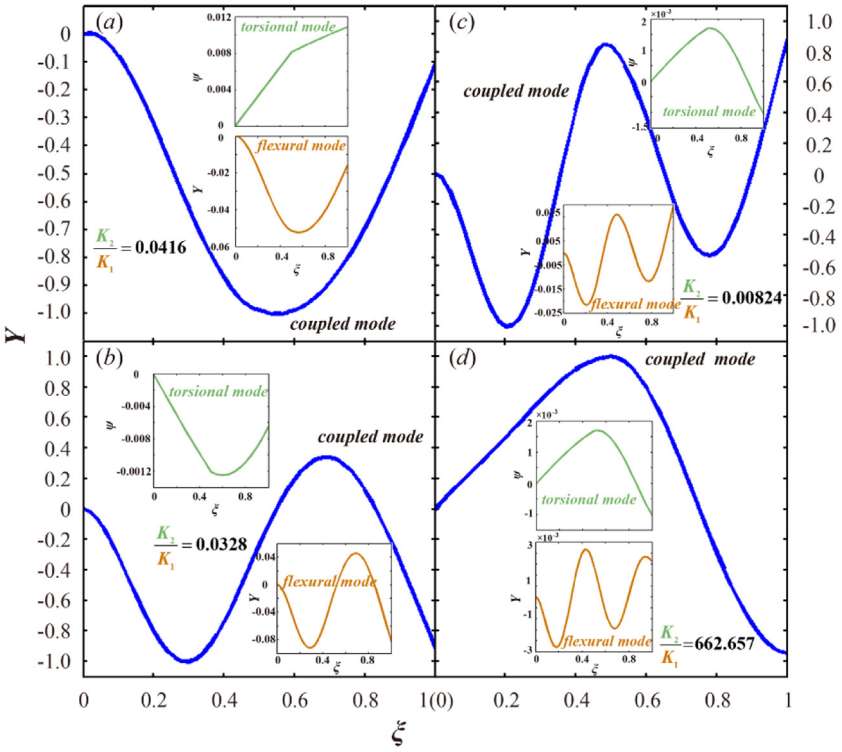

Fig. 5. The first four mode shapes with $\alpha_1 = 80$ ((a) the first mode, (b) the second mode, (c) the third mode, (d) the fourth mode). The large diagrams are the contact resonance mode shapes, the orange insets are the flexural mode shapes, and the green insets are the torsional mode shapes. . (For interpretation of the references to color in this figure legend, the reader is referred to the web version of this article.)

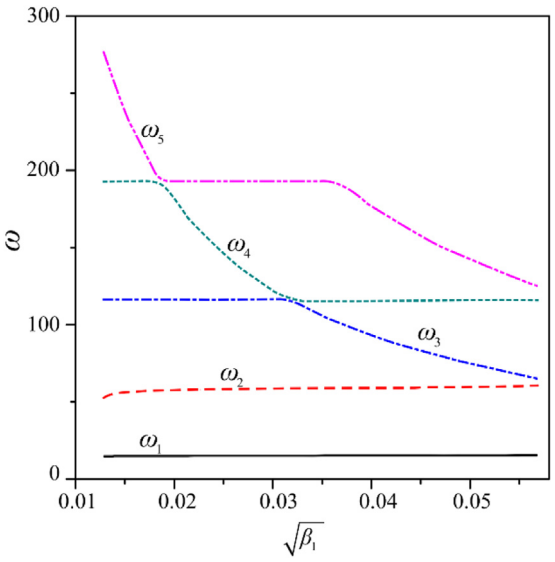

Fig. 6. Contact resonance frequencies (ω) as a function of the coupled factor $\sqrt{\beta_1}$.

the bifurcation point *O*. There is a sudden change of the 3rd and 4th eigenfrequencies before and after point *O*. A similar variation is obtained in the finite element analysis, and the details of which are given in Appendix C. When α_1 is low, the resonance frequencies gradually increase with the increasing α_1. For a larger value of α_1, the frequencies change little with the increasing α_1 [2]. The instability of the resonance frequency at point *O* is a result of the competition between the flexural and the torsional modes. In the contact mode, the flexural and torsional modes are coupled. These two types of vibrational modes compete with each other, and one of them dominates the coupled mode. The bifurcation occurs in higher coupled mode (3rd and 4th modes), and the lower order coupled modes (1st and 2nd modes) are stable. One reason is that the eigenfrequency of the first torsional mode is much higher than that of the first flexural mode [28]. Therefore, the first two contact resonance frequencies are stable due to less coupling. The insets in Fig. 3 are the mode shapes of the cantilever with different α_1s. Through the mode shapes, the dominant mode of the contact resonance frequency is easy to be identified, which is illustrated in the subsequent Figs. 4 and 5.

The first four mode shapes are shown in Figs. 4 and 5 with $\alpha_1 = 20$ and $\alpha_1 = 80$, respectively. In Figs. 4 and 5, the large diagrams are the coupled vibrational mode shapes, the orange insets are the flexural mode shapes, and the green insets are the torsional mode shapes. To better demonstrate the dominant vibrational mode in a coupled mode, the parameter K_2/K_1 is introduced to quantify the contribution of the torsional mode and the flexural mode to the coupled mode. Here $K_1 = \int_0^1 Y_i^2(\xi)d\xi$ and $K_2 = \int_0^1 \psi_i^2(\xi)d\xi$, ($i = 1$ and 2). When the value of $K_2/K_1 \ll 1$, the contact resonance frequency is dominated by the flexural vibration. While the value of $K_2/K_1 \gg 1$, the contact resonance frequency is dominated by the torsional vibration. As seen in Fig. 4(c), K_2/K_1 is 82.210, much larger than 1, the third contact resonance frequency is dominated by the torsional vibration when α_1 is 20. Whereas in Fig. 5(c), K_2/K_1 is 0.00824, much less than 1, the third contact resonance frequency is dominated by the flexural vibration when α_1 is 80. Therefore, in Fig. 3, in the region before point *O*, the third contact resonance frequency of the T-shape cantilever is dominated by the first torsional mode. And it is dominated by the fourth flexural mode in the region after point *O*. A strong coupling occurs at the bifurcation point *O*. A transformation of the dominant mechanism is completed at point *O*.

In Figs. 4 and 5, the dominance of a mode can be easily seen by showing the coupled mode together with the flexural and torsional modes. The parameter $\sqrt{\beta_1}$ is introduced in Fig. 6 to indicate the coupling relation between the flexural and the torsional modes. Here $\sqrt{\beta_1} = \sqrt{\frac{EI_1/L^3}{\rho A_1 L}\frac{\rho I_{P1} L}{GJ_1/L}}$ and $\sqrt{\beta_1}$ determines the likelihood of mode coupling. As the cantilever design, which is embodied in $\sqrt{\beta_1}$, determines this mode coupling behavior [35], the contact resonance frequency ω as a function of $\sqrt{\beta_1}$ is shown in Fig. 6. Here the ω_n on the curve represents the *n*th resonance frequency. As seen in Fig. 6, the frequencies of the fourth mode and the fifth mode rapidly approach each other and then diverge without crossing around $\sqrt{\beta_1} = 0.018$, which is the so-called eigenvalue curve veering phenomenon [36,37]. The same thing occurs for the frequencies of the third mode and the fourth mode around $\sqrt{\beta_1} = 0.031$. Similarly, Reinstädler et al. demonstrated with experiments that "the frequencies of the third flexural mode and the first torsional mode lie within 5% of each other" at $\sqrt{\beta_1} = 0.025$ [35], which is also theoretically confirmed by Hurley et al. [5]. The loci difference of the eigenvalue curve veering, i.e., $\sqrt{\beta_1}$, between this study and the study of Reinstädler et al. is caused by the difference of cantilever geometrical parameter. The occurrence of the eigenvalue curve veering suggests that at certain areas the system is very sensitive to $\sqrt{\beta_1}$. The eigenvalue curve veering is due to (strong) coupling, which usually results in the rapid and even violent changes in mode shape and eigenfrequency [36,37]. In summary, the eigenvalue curve veerings occur in ω_3/ω_4 and ω_4/ω_5 but not in ω_1/ω_2 in Fig. 6. As there is no eigenvalue curve veering in ω_1/ω_2 and thus indicates little mode coupling/interaction, this is (partly) responsible for that there is no bifurcation for the first two contact resonance frequencies as shown in Fig. 3.

For simplicity, damping is not considered in our model of Eqs. (1) and (2). The damping influence on the contact resonance frequency ω (λ_f^2) as a function of α_1 is examined in Fig. 7. The detailed computation procedures of the damped cantilever model are given in Appendix B. The influence of damping is little with the moderate damping parameters, which are taken from the experiment [1] and given in Appendix B. As seen in Fig. 7, the two curves almost overlap, the curves of the first two modes change continuously, and the α_1 value for the third mode bifurcation point is (almost) the same. Stan et al. found that the contact resonance frequency depends almost entirely on elastic modulus [38]. Therefore, the previous theoretical analysis based on an undamped T-shaped cantilever is applicable in practice.

As shown Eq. (11), the elastic properties of sample are contained in the parameters of α_1 and α_4. These two parameters have the following relation: $\alpha_4/\alpha_1 = (k_L/k_n)(EI_2/GJ_2)$. Here $k_L/k_n \approx 2(1-\upsilon_s)/(2-\upsilon_s)$ [39]. Fig. 8 shows the Poisson's ratio υ_s of sample as a function of α_1 with different geometrical parameters of the T-shaped cantilever. Here α_1 is the value at the corresponding bifurcation point. The α_1-υ_s plots in Fig. 8 are obtained by solving for the determinant of the matrix **A** to be zero and combining the relation between the α_1 and α_4 as follows: $\alpha_4/\alpha_1 \approx \left[2(1-\upsilon_s)/(2-\upsilon_s)\right](EI_2/GJ_2)$. As seen in Fig. 8, there is a one-to-one relation between the υ_s and the α_1 for a known cantilever. That is, for a T-shape cantilever with known geometrical parameters, the value of α_1 at the bifurcation point is only affected by the Poisson's ratio of sample. Once the α_1 of bifurcation point is obtained in experiment, the Poisson's ratio of sample can be derived. Then Young's modulus and Poisson's ratio of sample can be decoupled. The Young's modulus of sample is derived. In Fig. 8, for a T-shape cantilever with the length ratio of $\xi_o = 0.9$ and width ratio of $\zeta = 2.5$, the α_1 values of bifurcation point are between 65 and 70. The results here match those in Fig. 3.

The bifurcation point is vital in this study, an issue remains: How to identify this bifurcation point in an experiment? As discussed above, the eigenfrequency and mode shape experience dramatic changes around the bifurcation point. As the result, the AFM response will also experience a dramatic change, which is a benchmark characteristics for an experiment to catch. This is the similar scenario to that by Albrecht

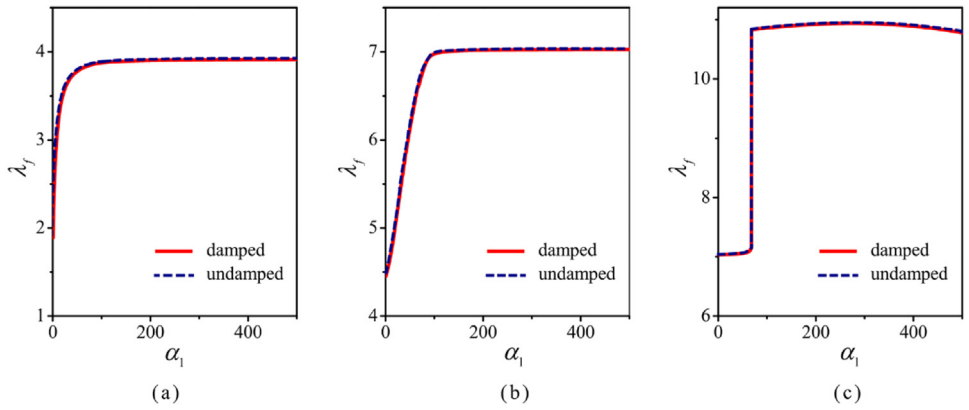

Fig. 7. Influence of damping on the contact resonance frequency ω $\left(\lambda_f = \sqrt{\omega}\right)$ as the α_1 value increases. (a) the first mode, (b) the second mode and (c) the third mode.

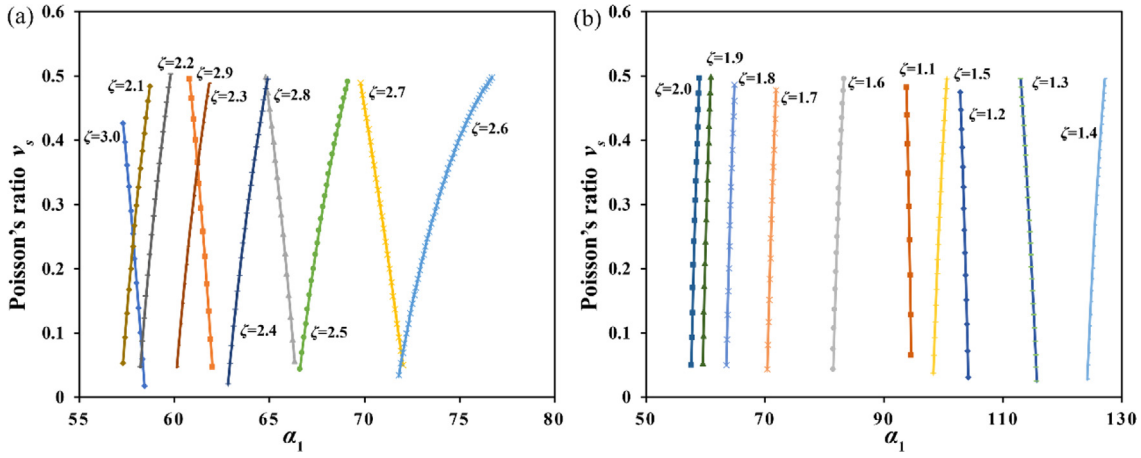

Fig. 8. The Poisson's ratio of the sample as a function of the α_1 at the bifurcation point. Here the width ratio $\zeta = b_2/b_1$ ranging from 1.1 to 3.0.

et al. [40], in which an AFM (tip) approaches a substrate. Because of the nonlinear interaction of the Lennard-Jones potential between the AFM tip and substrate, the AFM resonant frequency shifts and thus leads to the dramatic variation of the AFM frequency response, which is easily captured by the AFM vibration data in time series [40].

4. Conclusions

At the bifurcation point of resonance frequencies, the Poisson's ratio and the Young's modulus can be determined by a T-shape contact resonance atomic force microscopy. The flexural and torsional modes are simultaneously excited due to the tip away from the center axis, and these two vibrational modes are coupled in the contact mode. The eigenvalue curve veering phenomena are seen for some mode. The eigenvalue curve veering is due to coupling, which usually results in the rapid and even violent changes in mode shape and eigenfrequency. A contact resonance frequency bifurcation occurs in higher mode (the third mode or higher), and it is a result of the competition between the flexural and torsional modes. An important finding is that the bifurcation point plays a pivotal role to decouple the Poisson's ratio and the Young's modulus. There is a one-to-one relation between the Poisson's ratio and the α_1 at the bifurcation point for a known T-shape cantilever. Once the corresponding α_1 is obtained, the Poisson's ratio of sample is determined, then the elastic modulus of sample is derived. This efficient and accurate method for the characterization of various nanomaterials is helpful.

CRediT authorship contribution statement

Feifei Gao: Carried out the computation, Wrote the paper. **Yin Zhang:** Designed the research, Wrote the paper.

Declaration of competing interest

The authors declare that they have no known competing financial interests or personal relationships that could have appeared to influence the work reported in this paper.

Acknowledgments

This work was supported by the National Natural Science Foundation of China (NSFC Nos. 11772335), the Strategic Program Research Program (B) of the Chinese Academy of Sciences (XDB22020201), the National Key Research and Development Program of China (2016YFB1200602-09 and 2016YFB1200602-10).

Appendix A. The expression of matrix A

The matrix **A** is an 11×11 matrix due to $A_3 = 0$, and form of matrix **A** is given in Box I.

The above matrix **A** can be rewritten in the block matrix form as $\mathbf{A} = \begin{pmatrix} \mathbf{B} & \mathbf{C} \\ \mathbf{D} & \mathbf{E} \end{pmatrix}$.

$$
\mathbf{A}=\begin{bmatrix}
1 & 0 & 1 & 0 & 0 & 0 & 0 & 0 & 0 & 0 & 0\\
0 & 1 & 0 & 1 & 0 & 0 & 0 & 0 & 0 & 0 & 0\\
0 & 0 & 0 & 0 & -\cos(\lambda_f) & -\sin(\lambda_f) & \cosh(\lambda_f) & \sinh(\lambda_f) & 0 & 0 & 0\\
0 & 0 & 0 & 0 & \sin(\lambda_f)-\frac{\alpha_1}{\lambda_f^3}\cos(\lambda_f) & -\cos(\lambda_f)-\frac{\alpha_1}{\lambda_f^3}\sin(\lambda_f) & \sinh(\lambda_f)-\frac{\alpha_1}{\lambda_f^3}\cosh(\lambda_f) & \cosh(\lambda_f)-\frac{\alpha_1}{\lambda_f^3}\sinh(\lambda_f) & 0 & \frac{\alpha_1\alpha_2}{\lambda_f^3}\cos(\sqrt{\beta_2}\lambda_t) & \frac{\alpha_1\alpha_2}{\lambda_f^3}\sin(\sqrt{\beta_2}\lambda_t)\\
\cos(\lambda_f\xi_o) & \sin(\lambda_f\xi_o) & \cosh(\lambda_f\xi_o) & \sinh(\lambda_f\xi_o) & -\cos(\lambda_f\xi_o) & -\sin(\lambda_f\xi_o) & -\cosh(\lambda_f\xi_o) & -\sinh(\lambda_f\xi_o) & 0 & 0 & 0\\
-\sin(\lambda_f\xi_o) & \cos(\lambda_f\xi_o) & \sinh(\lambda_f\xi_o) & \cosh(\lambda_f\xi_o) & \sin(\lambda_f\xi_o) & -\cos(\lambda_f\xi_o) & -\sinh(\lambda_f\xi_o) & -\cosh(\lambda_f\xi_o) & 0 & 0 & 0\\
-\cos(\lambda_f\xi_o) & -\sin(\lambda_f\xi_o) & \cosh(\lambda_f\xi_o) & \sinh(\lambda_f\xi_o) & \zeta\cos(\lambda_f\xi_o) & \zeta\sin(\lambda_f\xi_o) & -\zeta\cosh(\lambda_f\xi_o) & -\zeta\sinh(\lambda_f\xi_o) & 0 & 0 & 0\\
\sin(\lambda_f\xi_o) & -\cos(\lambda_f\xi_o) & \sinh(\lambda_f\xi_o) & \cosh(\lambda_f\xi_o) & -\zeta\sin(\lambda_f\xi_o) & \zeta\cos(\lambda_f\xi_o) & -\zeta\sinh(\lambda_f\xi_o) & -\zeta\cosh(\lambda_f\xi_o) & 0 & 0 & 0\\
0 & 0 & 0 & 0 & \frac{\alpha_1\alpha_2\beta_3}{\sqrt{\beta_2}\lambda_t}\cos(\lambda_f) & \frac{\alpha_1\alpha_2\beta_3}{\sqrt{\beta_2}\lambda_t}\sin(\lambda_f) & \frac{\alpha_1\alpha_2\beta_3}{\sqrt{\beta_2}\lambda_t}\cosh(\lambda_f) & \frac{\alpha_1\alpha_2\beta_3}{\sqrt{\beta_2}\lambda_t}\sinh(\lambda_f) & 0 & -\sin(\sqrt{\beta_2}\lambda_t)+\frac{\alpha_3^2\alpha_4}{\sqrt{\beta_2}\lambda_t}\cos(\sqrt{\beta_2}\lambda_t) & \cos(\sqrt{\beta_2}\lambda_t)+\frac{\alpha_3^2\alpha_4}{\sqrt{\beta_2}\lambda_t}\sin(\sqrt{\beta_2}\lambda_t)\\
0 & 0 & 0 & 0 & 0 & 0 & 0 & 0 & \sin(\lambda_t\xi_o) & -\cos(\sqrt{\beta_2}\lambda_t\xi_o) & -\sin(\sqrt{\beta_2}\lambda_t\xi_o)\\
0 & 0 & 0 & 0 & 0 & 0 & 0 & 0 & \cos(\lambda_t\xi_o) & \kappa\sqrt{\beta_2}\sin(\sqrt{\beta_2}\lambda_t\xi_o) & -\kappa\sqrt{\beta_2}\cos(\sqrt{\beta_2}\lambda_t\xi_o)
\end{bmatrix}
$$

Box I.

$$
\mathbf{B}=\begin{bmatrix}
1 & 0 & 1 & 0 & 0 & 0 & 0 & 0\\
0 & 1 & 0 & 1 & 0 & 0 & 0 & 0\\
0 & 0 & 0 & 0 & -\cos(\lambda_f) & -\sin(\lambda_f) & \cosh(\lambda_f) & \sinh(\lambda_f)\\
0 & 0 & 0 & 0 & \sin(\lambda_f)-\frac{\alpha_1}{\lambda_f^3}\cos(\lambda_f) & -\cos(\lambda_f)-\frac{\alpha_1}{\lambda_f^3}\sin(\lambda_f) & \sinh(\lambda_f)-\frac{\alpha_1}{\lambda_f^3}\cosh(\lambda_f) & \cosh(\lambda_f)-\frac{\alpha_1}{\lambda_f^3}\sinh(\lambda_f)\\
\cos(\lambda_f\xi_o) & \sin(\lambda_f\xi_o) & \cosh(\lambda_f\xi_o) & \sinh(\lambda_f\xi_o) & -\cos(\lambda_f\xi_o) & -\sin(\lambda_f\xi_o) & -\cosh(\lambda_f\xi_o) & -\sinh(\lambda_f\xi_o)\\
-\sin(\lambda_f\xi_o) & \cos(\lambda_f\xi_o) & \sinh(\lambda_f\xi_o) & \cosh(\lambda_f\xi_o) & \sin(\lambda_f\xi_o) & -\cos(\lambda_f\xi_o) & -\sinh(\lambda_f\xi_o) & -\cosh(\lambda_f\xi_o)\\
-\cos(\lambda_f\xi_o) & -\sin(\lambda_f\xi_o) & \cosh(\lambda_f\xi_o) & \sinh(\lambda_f\xi_o) & -\zeta\sin(\lambda_f\xi_o) & \zeta\cos(\lambda_f\xi_o) & -\zeta\cosh(\lambda_f\xi_o) & -\zeta\sinh(\lambda_f\xi_o)\\
\sin(\lambda_f\xi_o) & -\cos(\lambda_f\xi_o) & \sinh(\lambda_f\xi_o) & \cosh(\lambda_f\xi_o) & -\zeta\sin(\lambda_f\xi_o) & \zeta\cos(\lambda_f\xi_o) & -\zeta\sinh(\lambda_f\xi_o) & -\zeta\cosh(\lambda_f\xi_o)
\end{bmatrix},
$$

Box II.

Here B is as given in Box II ,

$$
\mathbf{C}=\begin{bmatrix}
0 & 0 & 0\\
0 & 0 & 0\\
0 & 0 & 0\\
0 & \frac{\alpha_1\alpha_2}{\lambda_f^3}\cos(\sqrt{\beta_2}\lambda_t) & \frac{\alpha_1\alpha_2}{\lambda_f^3}\sin(\sqrt{\beta_2}\lambda_t)\\
0 & 0 & 0\\
0 & 0 & 0\\
0 & 0 & 0\\
0 & 0 & 0
\end{bmatrix},
$$

$$
\mathbf{E}=\begin{bmatrix}
0 & -\sin(\sqrt{\beta_2}\lambda_t)+\frac{\alpha_3^2\alpha_4}{\sqrt{\beta_2}\lambda_t}\cos(\sqrt{\beta_2}\lambda_t) & \cos(\sqrt{\beta_2}\lambda_t)+\frac{\alpha_3^2\alpha_4}{\sqrt{\beta_2}\lambda_t}\sin(\sqrt{\beta_2}\lambda_t)\\
\sin(\lambda_t\xi_o) & -\cos(\sqrt{\beta_2}\lambda_t\xi_o) & -\sin(\sqrt{\beta_2}\lambda_t\xi_o)\\
\cos(\lambda_t\xi_o) & \kappa\sqrt{\beta_2}\sin(\sqrt{\beta_2}\lambda_t\xi_o) & -\kappa\sqrt{\beta_2}\cos(\sqrt{\beta_2}\lambda_t\xi_o)
\end{bmatrix}.
$$

D is as given in Box III.

The determinant of the block matrix satisfies the following relation: $|\mathbf{A}| = |\mathbf{B}|\left|\mathbf{E}-\mathbf{D}\mathbf{B}^{-1}\mathbf{C}\right|$. Here matrix $\mathbf{B}$ is an invertible square matrix. Therefore, the $|\mathbf{A}| = 0$ is equivalent to the $\left|\mathbf{E}-\mathbf{D}\mathbf{B}^{-1}\mathbf{C}\right| = 0$. And the following equation is obtained

$$f_1(\alpha_1,\lambda_f)-f_2(\lambda_f)=0 \tag{A.1}$$

Here the $f_1(\alpha_1,\lambda_f)$ is a function of both the contact stiffness and the contact resonance frequency, and the $f_2(\lambda_f)$ is a function of the contact resonance frequency.

$$f_1(\alpha_1,\lambda_f)=\frac{\alpha_3^2\alpha_4-\alpha_1^2\alpha_2^2\beta_3 T}{\sqrt{\beta_2}\lambda_t},$$

$$T=\frac{g_1(\lambda_f)}{g_2(\lambda_f)+\alpha_1 g_3(\lambda_f)},$$

$$
\begin{aligned}
g_1(\lambda_f) = &-\{4(1-\zeta^2)\,[\sinh(\lambda_f(\xi_o-1))(\cos(\lambda_f+\beta_2\lambda_t-\lambda_f\xi_o)\\
&+\cos(\lambda_f-\beta_2\lambda_t-\lambda_f\xi_o))+\cosh(\lambda_f(\xi_o-1))\\
&(\sin(\lambda_f+\beta_2\lambda_t-\lambda_f\xi_o)+\sin(\lambda_f-\beta_2\lambda_t-\lambda_f\xi_o))]\\
&+(\zeta-1)^2[\cosh(\lambda_f(\xi_o-1))(\sin(\lambda_f+\beta_2\lambda_t)+\sin(\lambda_f-\beta_2\lambda_t))\\
&+\sinh(\lambda_f(2\xi_o-1))(\cos(\lambda_f+\beta_2\lambda_t)+\cos(\lambda_f-\beta_2\lambda_t))\\
&+(\cosh(\lambda_f(2\xi_o-1))+\cosh(\lambda_f))(\sin(\lambda_f+\beta_2\lambda_t-2\lambda_f\xi_o)\\
&+\sin(\lambda_f-\beta_2\lambda_t-2\lambda_f\xi_o))+(\sinh(\lambda_f(2\xi_o-1))-\sinh(\lambda_f))\\
&\times(\cos(\lambda_f+\beta_2\lambda_t-2\lambda_f\xi_o)+\cos(\lambda_f-\beta_2\lambda_t-2\lambda_f\xi_o))]\\
&+[(\xi_o+3)^2-8][\cosh(\lambda_f)(\sin(\lambda_f+\beta_2\lambda_t)+\sin(\lambda_f-\beta_2\lambda_t))\\
&-\sin(\lambda_f)(\cos(\lambda_f+\beta_2\lambda_t)+\cos(\lambda_f-\beta_2\lambda_t))]\}\,/(\beta_2\lambda_t),
\end{aligned}
$$

$$
\begin{aligned}
g_2(\lambda_f) = &\,2\lambda_f^3\,\{4(1+\zeta^2)+4(1-\zeta^2)\,[\cosh((\xi_o-1)\lambda_f)\cos((\xi_o-1)\lambda_f)\\
&+\cos(\lambda_f\xi_o)\cosh(\lambda_f\xi_o)]\\
&+(\zeta-1)^2\,[\cos(\lambda_f(2\xi_o-1))\cosh(\lambda_f)+\cosh(\lambda_f(2\xi_o-1))\\
&\times\cos(\lambda_f)+\cos(\lambda_f(2\xi_o-1))\cosh(\lambda_f(2\xi_o-1))]\\
&+[(\zeta+3)^2-8]\cos\lambda_f\cosh\lambda_f\}
\end{aligned}
$$

$$
\begin{aligned}
g_3(\lambda_f) = &\,2\{\sinh\lambda_f\,[-(\zeta-1)^2\cos((2\xi_o-1)\lambda_f)\;-\;((\zeta+3)^2-8)\cos\lambda_f]\\
&+\cosh\lambda_f\,[-(\zeta-1)^2\sin((2\xi_o-1)\lambda_f)\\
&+((\zeta+3)^2-8)\sin\lambda_f]+\cosh((2\xi_o-1)\lambda_f)\\
&\times[-(\zeta-1)^2\sin((2\xi_o-1)\lambda_f)\;+\;(\zeta-1)^2\sin\lambda_f]\\
&+\sinh((2\xi_o-1)\lambda_f)\,[(\zeta-1)^2\cos((2\xi_o-1)\lambda_f)\;+(\zeta-1)^2\cos\lambda_f]\\
&+4(\zeta^2-1)\cosh((\xi_o-1)\lambda_f)\sin((\xi_o-1)\lambda_f)\\
&+4(1-\zeta^2)\sinh((\xi_o-1)\lambda_f)\cos\,((\xi_o-1)\lambda_f)\}
\end{aligned}
$$

$$
f_2(\lambda_f)=-\frac{\tan(\sqrt{\beta_2}\lambda_t)\left[\tan(\sqrt{\beta_2}\lambda_t\xi_o)-\kappa\sqrt{\beta_2}\tan(\lambda_t\xi_o)\right]+\kappa\sqrt{\beta_2}\tan(\sqrt{\beta_2}\lambda_t\xi_o)+1}{\tan(\sqrt{\beta_2}\lambda_t)\left[\kappa\sqrt{\beta_2}\tan(\sqrt{\beta_2}\lambda_t\xi_o)\tan(\lambda_t\xi_o)+1\right]-\tan(\sqrt{\beta_2}\lambda_t\xi_o)+\kappa\sqrt{\beta_2}\tan(\lambda_t\xi_o)},
$$

$$\lambda_t=\sqrt{\beta_1}\lambda_f^2.$$

$$\mathbf{D}=\begin{bmatrix} 0 & 0 & 0 & 0 & \frac{\alpha_1\alpha_2\beta_3}{\sqrt{\beta_2}\lambda_t}\cos(\lambda_f) & \frac{\alpha_1\alpha_2\beta_3}{\sqrt{\beta_2}\lambda_t}\sin(\lambda_f) & \frac{\alpha_1\alpha_2\beta_3}{\sqrt{\beta_2}\lambda_t}\cosh(\lambda_f) & \frac{\alpha_1\alpha_2\beta_3}{\sqrt{\beta_2}\lambda_t}\sinh(\lambda_f) \\ 0 & 0 & 0 & 0 & 0 & 0 & 0 & 0 \\ 0 & 0 & 0 & 0 & 0 & 0 & 0 & 0 \end{bmatrix},$$

Box III.

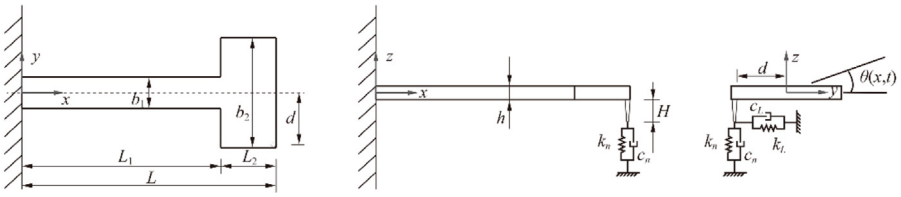

Fig. B.1. Schematic diagram of the AFM T-shape cantilever.

Appendix B. Model development and computation of a damped T-shape cantilever

For a T-shape cantilever in Fig. B.1, the governing equations are derived by applying the Hamilton's principle as follows [29]:

$$\begin{cases} m_1\dfrac{\partial^2 w_1}{\partial t^2}+EI_1\dfrac{\partial^4 w_1}{\partial x^4}+c_1\dfrac{\partial w_1}{\partial t}=0, & 0\le x\le L_1, \\ m_2\dfrac{\partial^2 w_2}{\partial t^2}+EI_2\dfrac{\partial^4 w_2}{\partial x^4}+c_1\dfrac{\partial w_2}{\partial t}+\delta(x-L)k_n(w_2-\theta_2 d) & \\ +\delta(x-L)c_n(\dfrac{\partial w_2}{\partial t}-\dfrac{\partial \theta_2}{\partial t}d)=0, & L_1\le x\le L. \end{cases} \tag{B.1}$$

$$\begin{cases} \rho I_{P1}\dfrac{\partial^2\theta_1}{\partial t^2}-GJ_1\dfrac{\partial^2\theta_1}{\partial x^2}+c_1\dfrac{\partial\theta_1}{\partial t}=0, & 0\le x\le L_1, \\ \rho I_{P2}\dfrac{\partial^2\theta_2}{\partial t^2}-GJ_2\dfrac{\partial^2\theta_2}{\partial x^2}+c_1\dfrac{\partial\theta_2}{\partial t}-\delta(x-L)k_n d(w_2-\theta_2 d) & \\ -\delta(x-L)c_n d(\dfrac{\partial w_2}{\partial t}-\dfrac{\partial\theta_2}{\partial t}d) & L_1\le x\le L. \\ +\delta(x-L)k_L H^2\theta_2+\delta(x-L)c_L H^2\dfrac{\partial\theta_2}{\partial t}=0, & \end{cases} \tag{B.2}$$

As the T-shape structure, the cantilever is divided into two parts, w_i, θ_i, m_i, EI_i, ρ, I_{Pi}, GJ_i (i = 1 and 2) denote the cantilever deflection, angle of twist, mass per unit length, flexural stiffness, density, polar area moment of the inertia and torsional stiffness of the two parts, respectively. The polar area moment of the inertia $I_{Pi}=(b_i h^3+b_i^3 h)/12$ (i = 1 and 2), and the torsional stiffness $GJ_i=\frac{1}{3}Gb_i h^3\left[1-0.63\frac{h}{b_i}+0.052\left(\frac{h}{b_i}\right)^3\right]$ (i = 1 and 2) [30]. Here k_n, k_L, c_n, c_L and c_1 are the vertical contact stiffness, the tangential contact stiffness, the damping coefficient for the vertical contact, the damping coefficient for the tangential contact and the cantilever damping coefficient, respectively.

The following quantities are introduced to nondimensionalize Eqs. (B.1) and (B.2)

$$\xi=x/L,\quad \xi_o=L_1/L,\quad W_1=w_1/L,\quad W_2=w_2/L,\quad \tau=\sqrt{EI_1/m_1L^4}\,t. \tag{B.3}$$

where $\sqrt{EI_1/m_1L^4}$ is with the unit of Hertz and it is the same order of the first natural frequency of a uniform and undamped cantilever [33].

Eqs. (B.1) and (B.2) now become the following dimensionless ones:

$$\begin{cases} \dfrac{\partial^2 W_1}{\partial\tau^2}+\dfrac{\partial^4 W_1}{\partial\xi^4}+C\dfrac{\partial W_1}{\partial\tau}=0, & 0\le\xi\le\xi_o, \\ \dfrac{\partial^2 W_2}{\partial\tau^2}+\dfrac{\partial^4 W_2}{\partial\xi^4}+\dfrac{C}{\zeta}\dfrac{\partial W_2}{\partial\tau}+\delta(\xi-1)[\alpha_1(W_2-\alpha_2\theta_2) & \\ +\alpha_5(\dfrac{\partial W_2}{\partial\tau}-\alpha_2\dfrac{\partial\theta_2}{\partial\tau})=0], & \xi_o\le\xi\le 1. \end{cases} \tag{B.4}$$

$$\begin{cases} \dfrac{\partial^2\theta_1}{\partial\xi^2}-\beta_1\dfrac{\partial^2\theta_1}{\partial\tau^2}-C\beta_4\dfrac{\partial\theta_1}{\partial\tau}=0, & 0\le\xi\le\xi_o, \\ \dfrac{\partial^2\theta_2}{\partial\xi^2}-\beta_1\beta_2\dfrac{\partial^2\theta_2}{\partial\tau^2}-C\beta_5\dfrac{\partial\theta_2}{\partial\tau}+\delta(\xi-1)\alpha_2\beta_3 & \\ [\alpha_1(W_2-\alpha_2\theta_2)+\alpha_5(\dfrac{\partial W_2}{\partial\tau}-\alpha_2\dfrac{\partial\theta_2}{\partial\tau})] & \xi_o\le\xi\le 1. \\ -\delta(\xi-1)\alpha_3^2[\alpha_4\theta_2+\alpha_6\beta_3\dfrac{\partial\theta_2}{\partial\tau}]=0, & \end{cases} \tag{B.5}$$

Here ζ is the width ratio of the two parts defined as $\zeta=b_2/b_1$, $C=c_1\sqrt{L^4/m_1EI_1}$ indicates the damping influence. And $\alpha_i s$ (i = 1 to 6) are defined as

$$\alpha_1=k_nL^3/EI_2,\quad \alpha_2=d/L,\quad \alpha_3=H/L,\quad \alpha_4=k_LL^3/GJ_2,$$
$$\alpha_5=(c_n/L)\sqrt{L^4/m_2EI_2},\quad \alpha_6=(c_L/L)\sqrt{L^4/m_2EI_2}. \tag{B.6}$$

Physically α_1 is the ratio of the vertical contact stiffness to the cantilever flexural stiffness and α_4 is the ratio of the tangential contact stiffness to the cantilever torsional stiffness. Here α_2 is the ratio of the off-center distance to the total cantilever length. α_3 is the ratio of the tip height to the total cantilever length. α_5 and α_6 indicate the damping influence.

Besides, $\beta_i s$ (i = 1 to 5) are defined as

$$\beta_1=\frac{EI_1/L^3}{\rho A_1 L}\frac{\rho I_{P1}L}{GJ_1/L},\quad \beta_2=\frac{I_{P2}}{I_{P1}}\frac{GJ_1}{GJ_2},\quad \beta_3=\frac{EI_2}{GJ_2},\quad \beta_4=\frac{EI_1}{GJ_1L^2},$$
$$\beta_5=\frac{EI_1}{GJ_2L^2}. \tag{B.7}$$

Here, $\sqrt{\beta_1}$ indicates the likelihood of modal coupling. β_2 is the ratio of the polar area moment of the inertia to the torsional stiffness. β_3, β_4 and β_5 are the ratios of the flexural stiffness to the torsional stiffness.

The Galerkin method is used to compute the Eqs. (B.4) and (B.5), $W_i(\xi,\tau)$ and $\theta_i(\xi,\tau)$ (i = 1 and 2) are assumed as follows:

$$W_i(\xi,\tau)=\sum_{k=1}^{N}a_k(\tau)Y_{ik}(\xi),\quad \theta_i(\xi,\tau)=\sum_{k=1}^{N}a_k(\tau)\psi_{ik}(\xi). \tag{B.8}$$

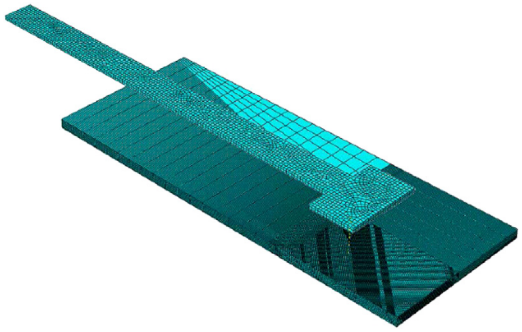

Fig. C.1. The finite element analysis of a T - shape cantilever in the contact mode. In this example, the cantilever has a total length $L = 300$ μm, width $b_1 = 20$ μm, $b_2 = 50$ μm, thickness $h = 3$ μm, and length ratio $\xi_o = 0.9$. The tip has a radius of 100 nm. The length, width and thickness of the sample are 250 μm, 100 μm and 6 μm, respectively.

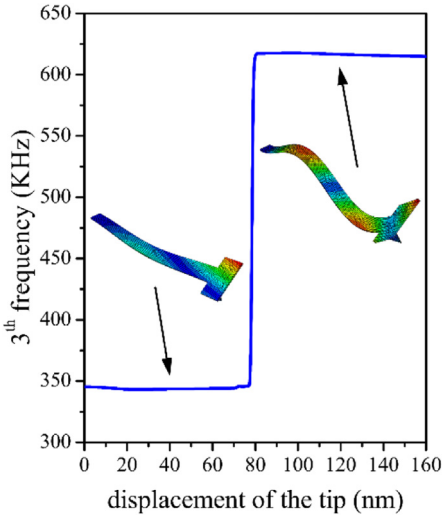

Fig. C.2. The third eigenfrequency as a function of the tip displacement. The insets are the corresponding mode shapes at different displacements of the tip.

Here $a_k(\tau)$ is the amplitude to be determined, N is the mode number, $Y_{ik}(\xi)$ and $\psi_{ik}(\xi)$ are the mode shapes of the T-shape cantilever that obtained from the previous calculation. Substitute Eq. (B.8) into Eq. (B.4), time $Y_{ij}(\xi)$ and integrate from 0 to 1, the governing equation is derived as follows:

$$\mathbf{M}\ddot{\mathbf{X}} + \mathbf{C}\dot{\mathbf{X}} + \mathbf{K}\mathbf{X} = \mathbf{0} \tag{B.9}$$

Here $\mathbf{X} = \begin{bmatrix} a_1(\tau) & a_2(\tau) & \cdots & a_N(\tau) \end{bmatrix}^T$. And the following matrices $\mathbf{M}$, $\mathbf{C}$ and $\mathbf{K}$ are derived with the orthogonal property of the mode shapes.

$$\mathbf{M}_{kj} = \begin{cases} \int_0^{\xi_o} Y_{1k}^2(\xi)d\xi + \int_{\xi_o}^1 Y_{2k}^2(\xi)d\xi, & k = j, \\ 0, & k \neq j. \end{cases} \tag{B.10}$$

$$\mathbf{C}_{kj} = \begin{cases} C\int_0^{\xi_o} Y_{1k}^2(\xi)d\xi + \dfrac{C}{\zeta}\int_{\xi_o}^1 Y_{2k}^2(\xi)d\xi, & k = j, \\ \quad +\alpha_5\left[Y_{2k}^2(1) - \alpha_2 Y_{2k}(1)\psi_{2k}(1)\right] & \\ \alpha_5\left[Y_{2k}^2(1) - \alpha_2 Y_{2k}(1)\psi_{2k}(1)\right], & k \neq j. \end{cases} \tag{B.11}$$

$$\mathbf{K}_{kj} = \begin{cases} \lambda_f^4\left[\int_0^{\xi_o} Y_{1k}^2(\xi)d\xi + \int_{\xi_o}^1 Y_{2k}^2(\xi)d\xi\right], & k = j, \\ \quad +\alpha_1\left[Y_{2k}^2(1) - \alpha_2 Y_{2k}(1)\psi_{2k}(1)\right] & \\ \alpha_1\left[Y_{2k}^2(1) - \alpha_2 Y_{2k}(1)\psi_{2k}(1)\right], & k \neq j. \end{cases} \tag{B.12}$$

In order to solve natural frequencies, the Eq. (B.9) is now rewritten as follows:

$$\mathbf{M}^*\dot{\mathbf{Z}}(\tau) + \mathbf{K}^*\mathbf{Z}(\tau) = \mathbf{0}. \tag{B.13}$$

Here the matrices of $\mathbf{M}^*$, $\mathbf{K}^*$ and the vector of $\mathbf{Z}(\tau)$ are defined for a damped non-gyroscopic system as follows [34]:

$$\mathbf{M}^* = \begin{pmatrix} \mathbf{M} & \mathbf{0} \\ \mathbf{0} & -\mathbf{K} \end{pmatrix}, \quad \mathbf{K}^* = \begin{pmatrix} \mathbf{C} & \mathbf{K} \\ \mathbf{K} & \mathbf{0} \end{pmatrix}, \quad \mathbf{Z}(\tau) = \begin{pmatrix} \dot{\mathbf{X}}^T(\tau) \\ \mathbf{X}^T(\tau) \end{pmatrix}.$$

The contact resonance frequencies of the damped T-shape cantilever can be obtained from the eigenvalues of the Eq. (B.13). In Fig. 7, the following parameters are fixed as $C = 0.1$, $\alpha_5 = 0.5$ [1].

Appendix C. The finite element analysis model

Fig. C.1 shows a graphical depiction of the finite element analytical mode. Here, the cantilever and tip are made of silicon, whose density, Young's modulus and Poisson's ratio are 2330 kg/m^3, 160.5 GPa and 0.168, respectively. The density, Young's modulus and Poisson's ratio of the sample are 1050 kg/m^3, 3.5 GPa and 0.35, respectively [41]. Fig. C.2. shows that the third eigenfrequency is related to the vertical displacement of the tip.

References

[1] A. Caron, W. Arnold, Observation of local internal friction and plasticity onset in nanocrystalline nickel by atomic force acoustic microscopy, Acta Mater. 57 (2009) 4353–4363, http://dx.doi.org/10.1016/j.actamat.2009.05.030.
[2] D.C. Hurley, J.A. Turner, Measurement of Poisson's ratio with contact-resonance atomic force microscopy, J. Appl. Phys. 102 (2007) 033509, http://dx.doi.org/10.1063/1.2767387.
[3] D.C. Hurley, M. Kopycinska-Müller, E.D. Langlois, A.B. Kos, N. Barbosa III, Mapping substrate/film adhesion with contact-resonance-frequency atomic force microscopy, Appl. Phys. Lett. 89 (2006) 021911, http://dx.doi.org/10.1063/1.2221404.
[4] X. Zhou, J. Fu, F. Li, Contact resonance force microscopy for nanomechanical characterization: Accuracy and sensitivity, J. Appl. Phys. 114 (2013) 064301, http://dx.doi.org/10.1063/1.4817659.
[5] J.A. Turner, D.C. Hurley, Ultrasonic methods in contact atomic force microscopy, Methods 3 (2003) 117–148.
[6] T. Wang, C. Fu, F. Xu, Y. Huo, M. Potier-Ferry, On the wrinkling and restabilization of highly stretched sheets, Internat. J. Engrg. Sci. 136 (2019) 1–16, http://dx.doi.org/10.1016/j.ijengsci.2018.12.002.
[7] J.J. Vlassak, W.D. Nix, A new bulge test technique for the determination of Young's modulus and Poisson's ratio of thin films, J. Mater. Res. 7 (1992) 3242–3249, http://dx.doi.org/10.1557/JMR.1992.3242.
[8] W.C. Oliver, G.M. Pharr, An improved technique for determining hardness and elastic modulus using load and displacement sensing indentation experiments, J. Mater. Res. 7 (1992) 1564–1583, http://dx.doi.org/10.1557/JMR.1992.1564.
[9] Y. Cao, X. J, X. Feng, On determination of the damping factor of linear viscoelastic materials using dynamic indentation: a theoretical study, Sci. China Phys. Mech. 54 (2011) 598–605, http://dx.doi.org/10.1007/s11433-011-4279-z.
[10] Y. Zhang, F. Gao, Z. Zheng, Z. Cheng, An inverse problem in film/substrate indentation: extracting both the Young's modulus and thickness of films, Acta Mech. Sin. 34 (2018) 1061–1071, http://dx.doi.org/10.1007/s10409-018-0778-8.
[11] Y. Zhang, Y. Zhao, Z. Cheng, Determining the layers' Young's moduli and thickness from the indentation of a bilayer structure, J. Phys. D Appl. Phys. 51 (2018) 065305, https://orcid.org/0000-0001-5334-0605.
[12] W.C. Oliver, G.M. Pharr, Measurement of hardness and elastic modulus by instrumented indentation: Advances in understanding and refinements to methodology, J. Mater. Res. 19 (2004) 3–20, http://dx.doi.org/10.1557/jmr.2004.19.1.3.
[13] J. Hsu, L. Chao, J. Jhong, T. Chen, W. Tsai, Determining the mechanical properties of optical films in liquid crystal displays (LCDs), Opt. Lasers Eng. 48 (2010) 354–360, http://dx.doi.org/10.1016/j.optlaseng.2009.10.007.
[14] G. Binnig, C.F. Quate, C. Gerber, Atomic force microscope, Phys. Rev. Lett. 56 (1986) 930–933, http://dx.doi.org/10.1103/PhysRevLett.56.930.
[15] S. Bradler, S.R. Kachel, A. Schirmeisen, B. Roling, A theoretical model for the cantilever motion in contact-resonance atomic force microscopy and its application to phase calibration in piezoresponse force and electrochemical strain microscopy, J. Appl. Phys. 120 (2016) 165107, http://dx.doi.org/10.1063/1.4964942.

[16] M. Aureli, S.N. Ahsan, R.H. Shihab, R.C. Tung, Plate geometries for contact resonance atomic force microscopy: Modeling, optimization, and verification, J. Appl. Phys. 124 (2018) 014503, http://dx.doi.org/10.1063/1.5038727.
[17] I. Kirrou, M. Belhaq, Contact stiffness modulation in contact-mode atomic force microscopy, Int. J. Nonlinear Mech. 55 (2013) 102–109, http://dx.doi.org/10.1016/j.ijnonlinmec.2013.04.013.
[18] A. Delnavaz, S.N. Mahmoodi, N. Jalili, H. Zohoor, Linear and non-linear vibration and frequency response analyses of microcantilevers subjected to tip–sample interaction, Int. J. Nonlinear Mech. 45 (2010) 176–185, http://dx.doi.org/10.1016/j.ijnonlinmec.2009.10.007.
[19] P.A. Yuya, D.C. Hurley, J.A. Turner, Contact-resonance atomic force microscopy for viscoelasticity, J. Appl. Phys. 104 (2008) 074916, http://dx.doi.org/10.1063/1.2996259.
[20] M. Natali, D. Passeri, M. Reggente, E. Tamburri, M.L. Terranova, M. Rossi, Contact resonance atomic force microscopy for viscoelastic characterization of polymer-based nanocomposites at variable temperature, AIP Conf. Proc. 1749 (2016) 020008, http://dx.doi.org/10.1063/1.4954491.
[21] R. Wagner, R.J. Moon, A. Raman, Mechanical properties of cellulose nanomaterials studied by contact resonance atomic force microscopy, Cellulose 23 (2016) 1031–1041, http://dx.doi.org/10.1007/s10570-016-0883-4.
[22] U. Andreaus, P. Baragatti, L. Placidi, Experimental and numerical investigations of the responses of a cantilever beam possibly contacting a deformable and dissipative obstacle under harmonic excitation, Int. J. Nonlinear Mech. 80 (2016) 96–106, http://dx.doi.org/10.1016/j.ijnonlinmec.2015.10.007.
[23] C. Ma, Y. Chen, W. Arnold, J. Chu, Detection of subsurface cavity structures using contact-resonance atomic force microscopy, J. Appl. Phys. 121 (2017) 154301, http://dx.doi.org/10.1063/1.4981537.
[24] Q. Tu, B. Lange, Z. Parlak, J.M.J. Lopes, V. Blum, S. Zauscher, Quantitative subsurface atomic structure fingerprint for 2D materials and heterostructures by first-principles-calibrated contact-resonance atomic force microscopy, ACS Nano 10 (2016) 6491–6500, http://dx.doi.org/10.1021/acsnano.6b02402.
[25] M. Reggente, D. Passeri, L. Angeloni, F.A. Scaramuzzo, M. Barteri, F. De Angelis, I. Persiconi, M.E. De Stefano, M. Rossi, Detection of stiff nanoparticles within cellular structures by contact resonance atomic force microscopy subsurface nanomechanical imaging, Nanoscale 9 (2017) 5671–5676, http://dx.doi.org/10.1039/C7NR01111C.
[26] J.P. Killgore, J.Y. Kelly, C.M. Stafford, M.J. Fasolka, D.C. Hurley, Quantitative subsurface contact resonance force microscopy of model polymer nanocomposites, Nanotechnology 22 (2011) 175706, http://dx.doi.org/10.1088/0957-4484/22/17/175706.
[27] K. Kimura, K. Kobayashi, A. Yao, H. Yamada, Visualization of subsurface nanoparticles in a polymer matrix using resonance tracking atomic force acoustic microscopy and contact resonance spectroscopy, Nanotechnology 27 (2016) 415707, http://dx.doi.org/10.1088/0957-4484/27/41/415707.
[28] O. Sahin, S. Magonov, C. Su, C.F. Quate, O. Solgaard, An atomic force microscope tip designed to measure time-varying nanomechanical forces, Nat. Nanotechnol. 2 (2007) 507–514, http://dx.doi.org/10.1038/nnano.2007.226.
[29] Y. Zhang, K.D. Murphy, Multi-modal analysis on the intermittent contact dynamics of atomic force microscope, J. Sound Vib. 330 (2011) 5569–5582, http://dx.doi.org/10.1016/j.jsv.2011.07.018.
[30] C.T.F. Ross, Finite Element Programs for Structural Vibrations, Springer, London, 1991.
[31] K.L. Johnson, Contact Mechanics, Cambridge University Press, Cambridge, 1985.
[32] R.W. Carpick, D.F. Ogletree, M. Salmeron, Lateral stiffness: a new nanomechanical measurement for the determination of shear strengths with friction force microscopy, Appl. Phys. Lett. 70 (1997) 1548, http://dx.doi.org/10.1063/1.118639.
[33] T.C. Chang, R.R. Craig, Normal modes of uniform beams, J. Eng. Mech. 95 (1969) 1027–1031.
[34] F. Gao, Y. Zhang, Enhancing the multiple harmonics by step-like cantilever, AIP Adv. 8 (2018) 045108, http://dx.doi.org/10.1063/1.5023623.
[35] M. Reinstaedtler, U. Rabe, V. Scherer, J.A. Turner, W. Arnold, Imaging of flexural and torsional resonance modes of atomic force microscopy cantilevers using optical interferometry, Surf. Sci. 532 (2003) 1152–1158, http://dx.doi.org/10.1016/S0039-6028(03)00183-3.
[36] A.W. Leissa, On a curve veering aberration, Z. Angew. Math. Phys. 25 (1974) 99–111, http://dx.doi.org/10.1007/BF01602113.
[37] C. Pierre, R.H. Plaut, Curve veering and mode localization in a buckling problem, Z. Angew. Math. Phys. 40 (1989) 758–761, http://dx.doi.org/10.1007/BF00945875.
[38] G. Stan, S.W. King, R.F. Cook, Nanoscale mapping of contact stiffness and damping by contact resonance atomic force microscopy, Nanotechnology 23 (2012) 215703, http://dx.doi.org/10.1088/0957-4484/23/21/215703.
[39] B. Bhushan, H. Fuchs, Applied Scanning Probe Methods II, Springer, Berlin, 2006.
[40] T.R. Albrecht, P. Grutter, D. Horne, D. Rugar, Frequency modulation detection using high-Q cantilevers for enhanced force microscope sensitivity, J. Appl. Phys. 69 (1991) 668, http://dx.doi.org/10.1063/1.347347.
[41] H.J. Sharahi, G. Shekhawat, V. Dravid, S. Park, P. Egberts, S. Kim, Contrast mechanisms on nanoscale subsurface imaging in ultrasonic AFM: Scattering of ultrasonic wave and contact stiffness of tip-sample, Nanoscale 9 (2017) 2330–2339, http://dx.doi.org/10.1039/C6NR09124E.